Non-spherical oscillations drive the ultrasound-mediated release from targeted microbubbles

Guillaume Lajoinie[1], Ying Luan[2], Erik Gelderblom[1], Benjamin Dollet[3], Frits Mastik[2], Heleen Dewitte[4], Ine Lentacker[4], Nico de Jong[2,5] & Michel Versluis [1]

Ultrasound-driven microbubbles are attractive for a variety of applications in medicine, including real-time organ perfusion imaging and targeted molecular imaging. In ultrasound-mediated drug delivery, bubbles decorated with a functional payload become convenient transport vehicles and offer highly localized release. How to efficiently release and transport these nanomedicines to the target site remains unclear owing to the microscopic length scales and nanoseconds timescales of the process. Here, we show theoretically how non-spherical bubble oscillations lead first to local oversaturation, thereby inducing payload release, and then to microstreaming generation that initiates transport. Experimental validation is achieved through ultra-high-speed imaging in an unconventional side-view at tens of nanoseconds timescales combined with high-speed fluorescence imaging to track the release of the payload. Transport distance and intrinsic bubble behavior are quantified and agree well with the model. These results will allow for optimizing the therapeutic use of targeted microbubbles for precision medicine.

[1] Physics of Fluids Group, Techmed Centre and MESA+ Institute for Nanotechnology, University of Twente, P.O. Box 217, AE Enschede 7500, The Netherlands. [2] Biomedical Engineering, Thoraxcenter, Erasmus MC, P.O. Box 2040, CA Rotterdam 3000, The Netherlands. [3] CNRS, LIPhy, Univ. Grenoble Alpes, Grenoble 38000, France. [4] Ghent Research Group on Nanomedicines, Laboratory of General Biochemistry and Physical Pharmacy, Faculty of Pharmaceutical Sciences, Ghent University, Ottergemse Steenweg 460, Ghent 9000, Belgium. [5] Acoustical Wavefield Imaging, Delft University of Technology, Postbus 5, AA Delft 2600, The Netherlands. Correspondence and requests for materials should be addressed to M.V. (email: m.versluis@utwente.nl)

Clinical ultrasound probably meets all essential requirements to be the ideal medical imaging modality: an excellent safety record, good imaging resolution and penetration depth, and a real-time, or even faster, acquisition speed. However, its specificity remains limited. Microbubble ultrasound contrast agents can alleviate this shortcoming. Clinical use of microbubbles has been made possible by their core physical property, namely resonance. Upon exposure to the oscillatory pressure variations of an ultrasound wave, compressibility of the gas core combined with inertia of the surrounding liquid leads to a mass-spring-like resonance behavior whose Minnaert eigen-frequency obeys an inverse relation with the bubble radius[1]. The unique acoustic properties of microbubbles that present a typical radius of $1-3\,\mu m$ have also been used for two decades to boost perfusion imaging in the clinic, making them unrivaled blood pool agents[2].

In vivo, microbubbles have to circulate in the blood stream until reaching the target area. Extensive efforts have therefore been put into enhancing the stability of microbubbles by coating them with polymers, proteins, or lipids. Among these coatings, phospholipid shells have been the most widely used owing to their high biocompatibility, flexibility, and enhanced non-linear acoustic properties[3]. Furthermore, a lipid coating can be easily functionalized, e.g. by including stealth capability by adding polyethylene glycol (PEG), which prevents interactions with the immune system and prolongs the circulation time[4]. Moreover, targeting ligands can be attached to the periphery of the shell to specifically recognize and adhere to diseased cells and tissues[5, 6], thereby bringing a molecular imaging dimension to the clinical use of microbubbles. The same ligands can also be used to load the microbubbles with various nanoconstructs, turning them into efficient microcarriers. The number of formulations for drug-loaded microbubbles has vastly expanded. These include a broad range of interfacial structures, from simple drugs loaded onto the bubble shell[7, 8] to more complex nanoconstructs that can entrap genes or chemotherapeutics[9, 10].

Driven near its resonance frequency, a bubble displays maximal radial response and generates secondary effects, such as harmonics and subharmonics[11, 12], streaming, acoustic radiation forces, shape instabilities[13], and non-spherical oscillations[14, 15]. These effects are of prime importance in applications such as cleaning, (bacterial) biofilms removal[16], mechanical destruction of thrombus[17] or tumors[18, 19] or inducing vessel wall permeation, e.g for blood brain barrier opening[20]. The combination of the mechanical action of targeted microbubbles adherent to a surface with the release of a drug payload is of great interest for therapeutic applications as medicine is becoming increasingly focused towards personalized[21] and localized therapy[22, 23].

Although there is convincing experimental evidence for controlled release of the payload, the physical mechanisms behind it remain unclear. Some attempts were made to explain these phenomena: Borden et al.[24] proposed that the surface area reduction leads to the expulsion of excessive shell material, which is, however, difficult to assess owing to the nanoseconds time-scales and nanometer length scales governing the problem. O'Brien et al.[25] attempted to explain the shedding in relation to bubble stability by looking at molecular viscosity, while Kwan et al.[26] concluded that the release could originate from a cyclic nucleation and aggregation of lipid folding events. This, however, is difficult to combine with the observation that shedding can occur within just a few ultrasound cycles[27].

Here, we take a major step forward, both in the experimental observation of the microbubble shedding and in its physical description within the relevant pressure regime[28]. Time-resolved observation of the release was performed in an unconventional side view, which allowed the visualization of the release in the relevant plane of sight. The setup combines two high-speed cameras in order to simultaneously record the bubble oscillations at a tens of nanoseconds timescale, together with high-speed fluorescence imaging of the release and transport of the bubble payload at a tens of microseconds timescale. To this end, a fluorescent dye (DiI) was incorporated into the bubble shell to serve as a model drug to unravel the release and transport mechanisms of the payload at a range of acoustic parameters. We also study the controlled release theoretically, where we show good agreement with the experimental observations. These observations shed light on the physical mechanisms involved in drug delivery with microbubbles, and demonstrate the importance of the physical environment for the efficacy of the controlled release.

Results

Microbubble dynamics theory and modeling. The dynamics of free bubbles is described by the Rayleigh−Plesset equation and has been investigated for a century. It can theoretically account for large oscillation amplitudes and water compressibility[29], non-adiabatic compression[30] and complex viscoelastic behavior of the bubble shell[31, 32]. In practice, however, microbubbles are never in free space and further modifications were made to the primary models to account for the presence of a substrate. The so-called method of images is such an example in potential flow theory that considers the substrate as an acoustic reflector and offers an easy way to account for its effect on the bubble dynamics[33]. More extended spherical models were developed[34, 35] and tested[36, 37] to investigate the effect of the distance between the bubble and the substrate. However, the present physical problem requires going beyond the spherical models by considering the non-spherical dynamics of microbubble oscillations and the subsequent release and transport of the bubble payload.

Successfully explaining the physical aspects involved in shedding from microbubbles implies an understanding and description of the microbubble oscillations without the constraint of spherical symmetry. In this section we therefore build a potential flow model based on a simple idealization of the flow kinematics for the microbubble dynamics near a substrate, where the bubble is allowed a non-spherical axisymmetric motion (see Fig. 1).

First, we evaluate the expected displacement of the substrate as a result of the arrival of ultrasound, which can be estimated from a no-slip boundary condition and from liquid compressibility. For the studied range of pressures $(150-400\,kPa)$ at a driving frequency of 1 MHz, the amplitude of motion of a water fluid particle induced by the ultrasound wave is not more than 50 nm[38]. Such a displacement is negligible as compared to the observed bubble oscillation amplitude that typically reaches a few
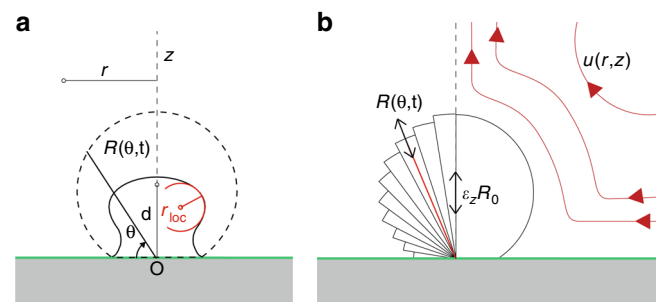
Fig. 1 Schematic description of the model. **a** Description of a bubble targeted to a substrate including the geometrical parameters. **b** The bubble undergoes volumetric oscillations and oscillatory translations under ultrasound exposure, thereby generating streaming

micrometers. Consequently, the displacement of a substrate with larger acoustic impedance is therefore also negligible. In addition, an oscillating bubble will preferentially displace water rather than inducing a local deformation of the substrate owing to the substrate's elasticity ($E = 3$ GPa for polystyrene). Thus, the substrate can then be identified as a rigid plane where we neglect its deformation along the contact area with the bubble. The center of this contact area is then taken as the origin to build our axisymmetric model. We now describe the radius R not only as a function of time but also of the elevation angle ϑ, Fig. 1a. Note that in the following the geometry used for the mathematical derivation remains spherical, since that condition is required to make use of the Rayleigh−Plesset dynamics. We consider in first approximation the velocity potential as radial in this coordinate system. The error associated with this assumption is discussed in Supplementary Note 1. This now allows us to rewrite the Rayleigh−Plesset equation in spherical coordinates (r, ϑ):

$$\rho_\ell \left(\ddot{R}(\vartheta, t) R(\vartheta, t) + \frac{3}{2}\dot{R}(\vartheta, t)^2 \right) = P_i(t) - P_e(t), \qquad (1)$$

with ρ_ℓ the liquid density, and $R(\vartheta, t)$ the time-dependent and angle-dependent radius with the overdots representing its time derivatives. P_i is the internal gas pressure:

$$P_i(t) = -\frac{4\mu_\ell \dot{R}(\vartheta, t)}{R(\vartheta, t)} - \frac{4\kappa_{R_0} \dot{R}(\vartheta, t)}{R(\vartheta, t)^2} - \Delta P(\vartheta, t) + P_0 \left(\frac{V(t)}{V_0} \right)^\gamma, \qquad (2)$$

and P_e is the external gas pressure:

$$P_e(t) = P_0 + P_A(t). \qquad (3)$$

Here, μ_ℓ is the liquid dynamic viscosity, P_0 is the ambient pressure, P_A is the applied ultrasound pressure, V is the bubble volume with V_0 the initial bubble volume, γ is the polytropic exponent of the gas, and κ_{R_0} is the shell viscosity. ΔP is the local pressure drop across the interface and the Young−Laplace equation is used to generalize the pressure drop due to surface tension:

$$\Delta P(\vartheta, t) = \sigma_w \left(\frac{1}{R_c(t)} + \frac{1}{r_{loc}(\vartheta, t)} \right), \qquad (4)$$

where σ_w is the surface tension of water, r_{loc} is the time-dependent local curvature on the bubble surface in the observation plane and R_c is the time-dependent radius of curvature in the orthogonal direction. The radius of curvature R_c can be estimated from the bubble volume $V = (4\pi R_c^3)/3$. The exact derivation of the curvature of the bubble and a discussion on this estimation can be found in Supplementary Note 2.

For numerical evaluation each bubble can be discretized and divided into angular segments of length $R = R(\vartheta, t)$ and width $d\vartheta$ that link the surface of the bubble to the origin at an elevation angle ϑ (see Fig. 1b). In general, each segment of the microbubble is considered to obey Eq. (1) and all segments together are coupled through the gas volume V, that in turn determines the internal gas pressure Eq. (2), and through r_{loc}, that is calculated using a finite difference method from the two closest neighbors. In many cases, the use of functionalized bubbles includes targeting to specific cell receptors. As a consequence, bubbles adhere to the functionalized supports upon contact and this adherence translates into the pinning of the triple line separating liquid, gas, and the substrate. The proposed way of modeling the non-spherical bubble dynamics gives a convenient and straight-forward way of handling this pinning by setting the velocity of the first segment to zero. The resulting set of differential equations

(one equation per segment) is then solved using the ODE113 solver in Matlab.

Describing the microbubble in this segmented picture has implications that we discuss in more detail now. First, the bubble volume being a summation of all segment volumes can be expressed as the sum of the volume fraction belonging to the segment with index i and the remaining volume V_r:

$$V = \frac{2\pi d\vartheta}{3} \sum_{j=1}^{n} R_j^3 \cos(\vartheta_j) = \frac{2\pi d\vartheta}{3} R_i^3 \cos(\vartheta_i) + V_r, \qquad (5)$$

with $d\vartheta$ the angle discretization step chosen for the model. When introducing Eq. (5) into Eq. (2), it becomes clear from Eq. (1) that (i) each segment will be a second-order oscillator whose eigenfrequency and phase behavior depends entirely on its initial length, identical to the Minnaert eigenfrequency of a spherical bubble. And (ii), that there is now an additional driving term V_r in Eq. (1) that is governed by the dynamics of all the other segments and that interferes (physically) with the original acoustic driving term. As a direct consequence of (i), the phase of the oscillations will increase for increasing initial segment length and therefore with increasing ϑ (see Supplementary Note 3). The segments with the smallest angles expand first, leading to an oblate shape during microbubble growth. The segments with the smallest angles also retract first, leading to a prolate shape upon collapse. This phase difference along the surface of the microbubble will prove crucial for both the release of the shell material and its subsequent transport.

The numerical model treats coupled oscillating segments and therefore allows for the existence of surface waves at the bubble interface. These surface waves are known to attenuate over a typical time that scales with the wavelength as λ^2 $\left(\tau = \lambda^2 \rho / 4\pi^2 \mu_\ell \right)$[33]. To account for this, we implement a damping correction for each segment in the numerical model with a damping term of the form $\kappa\dot{R}$:

$$\frac{\kappa}{(2R_0 d\vartheta)^2} \left(\dot{R}(\vartheta, t) - \frac{\dot{R}(\vartheta - d\vartheta, t) + \dot{R}(\vartheta + d\vartheta, t)}{2} \right), \qquad (6)$$

with $\kappa = 2.3 \times 10^{-5}\,\mathrm{m^2\,s^{-1}}$ the only empirical parameter of the model.

Non-spherical bubble oscillations. Figure 2a shows a typical radius−time curve $R_c(t)$ of a 3.9 μm radius targeted micro-bubble driven by a 100-cycle ultrasound pulse at a pressure of 166 kPa. The recording was taken at a frame rate near 7.5 million frames per second, and are shown here together with the simulated response at this pressure and for this particular bubble size. Figure 2b shows the corresponding simulated and measured contours $R(\vartheta, t)$. Figure 2c, d also shows simulated and experimental contours of microbubbles exposed to pressures of 249 and 331 kPa, respectively. Supplementary Movie 4 shows the simulated bubble dynamics for a 3.1-μm bubble exposed to 84, 166, and 210 kPa and Supplementary Movie 5 shows the simulated bubble dynamics for a 2.4, 3.1, and 4-μm bubble exposed to 210 kPa. From these contours, one can appreciate how the bubbles take an oblate shape while growing and a prolate shape while collapsing, as predicted. Such observations were made earlier[14, 15] and the physical explanation is now provided here.

Lipid oversaturation. An important implication of considering the phase as a function of the elevation angle is that the collapse of the bubble is now regarded as non-spherical. This becomes obvious when taking a closer look at the oscillation dynamics near the substrate, where the contact line is pinned. Until now,
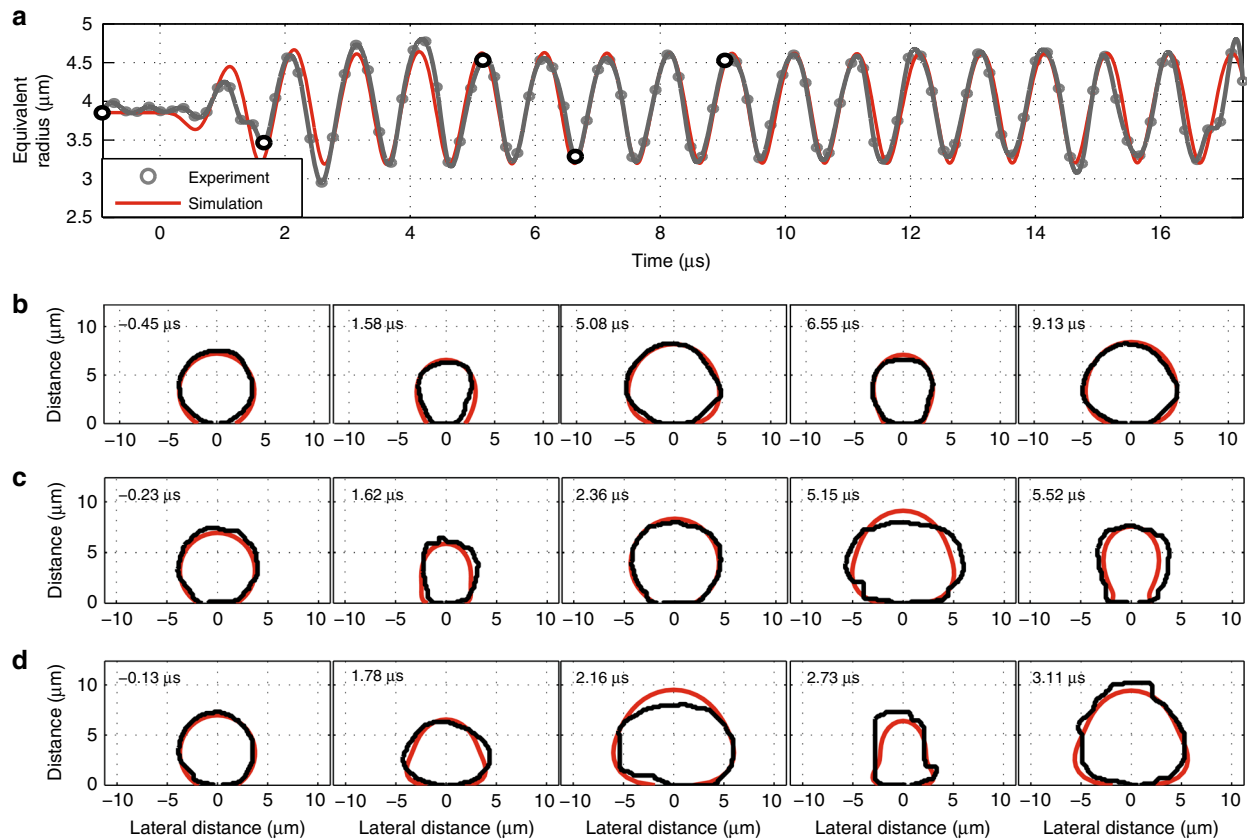
Fig. 2 Non-spherical microbubble oscillations. **a** Simulated and experimental radius−time curve $R_c(t)$ (as calculated from the time-dependent volume) of a 3.9 μm radius microbubble exposed to a 166 kPa ultrasound burst at a frequency of 1 MHz. **b** Snapshots of the simulated and experimental contours of the bubbles depicted in (**a**) at the times indicated by the circles. **c**, **d**. Snapshots of simulated and experimental contours of bubbles with similar radii exposed to pressures of 249 and 331 kPa, respectively. See Supplementary Movies 1 and 2 for the ultra-high-speed recordings of the non-spherical bubble oscillations and Supplementary Movie 3 for the details of the bubble dynamics simulation

ultrasound-mediated release mechanisms of lipids or nanoparticles from microbubbles have been described in the context of spherical oscillations alone[24–26] and the most commonly considered mechanism to explain detachment of the shell material from the surface of a microbubble involves oversaturation of the lipid layer due to the surface area reduction upon compression, as it is the most intuitive. As mentioned before, in practice, both in vitro and in vivo microbubbles are never in free space. In the free field, the total collapse of a spherical bubble is prevented by a rapid increase of pressure and temperature in the gas core. In the presence of highly non-spherical oscillations, however, the earlier collapse of the bubble segment at small elevation angles is not prevented by such a pressure increase, owing to the phase lag of the bubble segments at a larger elevation angle. Thus, given a sufficiently high acoustic driving pressure, one can expect that nothing prevents this particular segment of the bubble from fully collapsing. This cusp formation process is demonstrated in Fig. 3, showing a simulated lipid shell collapse for such a pinned microbubble for increasing pressures. From Fig. 3a it also becomes clear that the aspherical collapse leads to an oversaturation of phospholipids at a localized position between the cusp and the substrate. Plotted in an angle-resolved view, Fig. 3b shows the change in surface area of each segment in the collapse phase for increasing acoustic pressure. The corresponding increase in the local phospholipid concentration exceeds a factor of ten at pressures in excess of 166 kPa. Figure 3c also shows that the cusp formation becomes less pronounced for larger bubble sizes, away from resonance, as will be detailed in the following section.

Although it is well-known that the presence of a substrate can change bubble resonance behavior[34, 39], little investigations were performed on its effect on the sphericity of the oscillations in this pressure range and in this plane of observation. Unlike our preliminary study[27] where we studied microbubbles floating up against a substrate by buoyancy, here targeted microbubbles were used, resulting in the pinning of the area in contact with the Opticell™ membrane. It was found experimentally, see Supplementary Note 4, that the radius of the pinned contact line was on average half the bubble radius with no significant dependency on the bubble size or other quantifiable parameter. $r_{contact} = R_0/2$ was therefore used for the simulation. It should be kept in mind that there is a fair amount of variability and the contact radius can vary from 25% up to 70% of the bubble radius for the extreme cases. On the other hand, the size of the contact area has limited impact on the simulation output, see Supplementary Note 5. Even removing the pinning altogether (while the bubble kept contact with the substrate) in the simulation leads to the very same conclusions. With decreasing contact area the shape of the bubble at small ϑ angle turns from a cusp into a tip for which all the following arguments also apply. We note that this tip-like shape was observed before[15] for the bubbles presenting the smallest contact areas. Also, the pinning behavior of the targeted bubble did not change the previously observed release behavior[27], as confirmed by our preliminary experimental verifications and by the simulations.

Microstreaming and transport. It was proposed before that microstreaming surrounding the microbubble during ultrasound
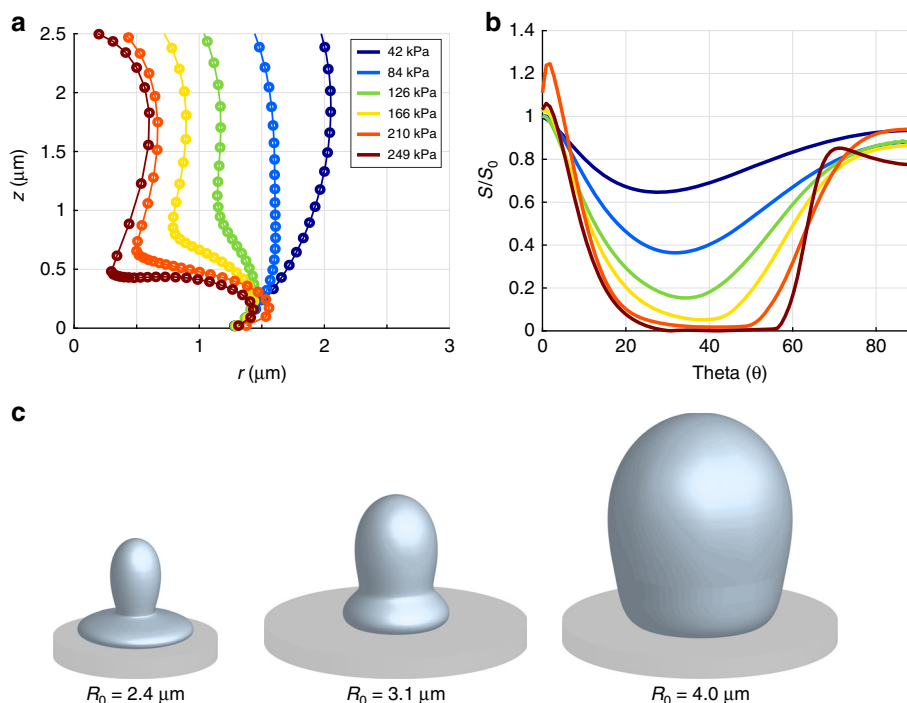
Fig. 3 Lipid oversaturation. **a** Shape of the cusp in the collapse phase for increasing pressures showing how the bubble ($R_0 = 2.4\,\mu m$) deforms and the phospholipids oversaturate. **b** Reduction in the surface area for the phospholipids in the compression phase for the same bubble size and for the same pressures as in (**a**) as a function of the elevation angle. **c** gives the simulated shape of the bubble in the compression phase for a targeted bubble with different initial radii driven at a pressure of 210 kPa. See Supplementary Movie 6 for an animation of the cusp formation and the corresponding surface area decrease
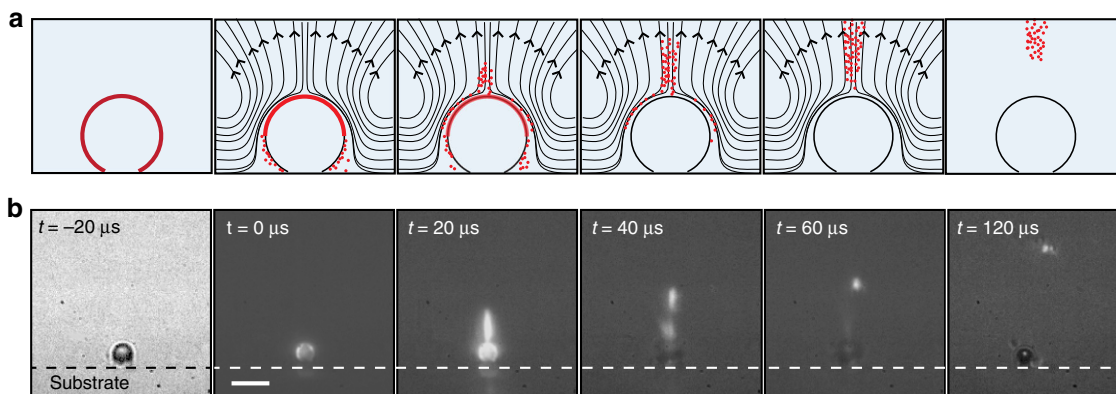
Fig. 4 Release and bubble streaming mechanism. **a** Schematics of the shedding process of the released material (red) with the calculated streamlines (solid black lines). **b** Experimental recording of the release of the fluorescent material from a targeted oscillating microbubble driven at a pressure of 331 kPa showing a clear transport over a distance several times larger than the bubble size. The fluorescence high-speed recording was taken in a side-view at 50,000 frames per second. Scale bar indicates a length of 10 μm. See Supplementary Movie 7 for a compilation of four high-speed fluorescence recordings showing the release and subsequent transport for different bubble sizes and different driving pressures

exposure is an important transport mechanism following the release events[27]. The axisymmetric velocity field resulting from simplified non-spherical bubble oscillations was calculated before by Marmottant and Hilgenfeldt[40] by assuming the bubble motion to be a superposition of a volumetric oscillation and an oscillatory translation perpendicular to the substrate and with a crucial phase difference $\Delta\varphi$ between the two. The resulting flow field, $u(r, z)$, see Fig. 1, is given by a combination of three Stokes singularities: a stokeslet (stk), a dipole (dip), and a hexadecapole (hexdp)[41].

The streamlines calculated for a 2.5 μm radius bubble exposed to a burst of 100 cycles at 1 MHz are shown in Fig. 4 and explain the trajectory followed by the released material: the phospholipids detach due to the local oversaturation near the substrate (see

subsection Lipid oversaturation) and are dragged along the microbubble surface with the local flow field. Once at the top of the bubble, the material is transported along the centerline (z-axis in our nomenclature) and away from the bubble as illustrated in Fig. 4a. The experimental evidence of this unintuitive behavior is captured in a side view recording using high-speed fluorescence imaging at a frame rate of 50,000 frames per second. Figure 4b shows a typical example of fluorescent material transported during several tens of microseconds. In about one third of the cases, a secondary pinched-off bubble, itself carrying some fluorescent material, was traveling along the central streamline together with the shed material without, however, having a measurable effect on the transport. The velocities observed were

typically of the order of $0.1\,\mathrm{m\,s}^{-1}$. The velocity of the fluorescently labeled molecules drops to zero as soon as ultrasound stops. This is a consequence of the highly viscous behavior of the surrounding water at these ultrashort length scales.

To describe the centerline transport along the z-axis ($r = 0$) the general flow field description $u(r, z)$ can be simplified to give:

$$u(z) = \epsilon_z \epsilon_R \sin(\Delta\varphi) R_0 \omega(\texttt{stk} + \texttt{dip} + \texttt{hexdp}), \quad (7)$$

where

$$\texttt{stk} = \frac{2}{\overline{z} - \overline{d}} - \frac{1}{\overline{z} + \overline{d}} - \frac{(\overline{z} - \overline{d})^2}{(\overline{z} + \overline{d})^3} - \frac{8\overline{d}\overline{z}}{(\overline{z} + \overline{d})^3}, \quad (8)$$

$$\texttt{dip} = -\left(\frac{1}{(\overline{z} - \overline{d})^3} - \frac{7}{(\overline{z} + \overline{d})^3} + \frac{6\overline{d}}{(\overline{z} + \overline{d})^4}\right), \quad (9)$$

$$\texttt{hexdp} = -\frac{1}{2}\left(\frac{1}{(\overline{z} - \overline{d})^6} - \frac{1}{(\overline{z} + \overline{d})^6}\right), \quad (10)$$

with z as described in Fig. 1, d the initial distance of the center of the bubble to the substrate, thus slightly smaller than the bubble radius due to the pinning, and where the overbars are used to indicate that the space variable is non-dimensionalized with the initial bubble radius R_0. ϵ_z and ϵ_R are the relative volumetric oscillation amplitudes and the relative oscillatory translation amplitudes, respectively, as defined in ref. [40]. The prefactor in Eq. (7) gives the typical velocity of the streaming and is proportional to the sine of the phase difference $\Delta\varphi$ between volumetric oscillations and oscillatory translations. Thus, in this description, streaming can indeed only arise from non-spherical oscillations.
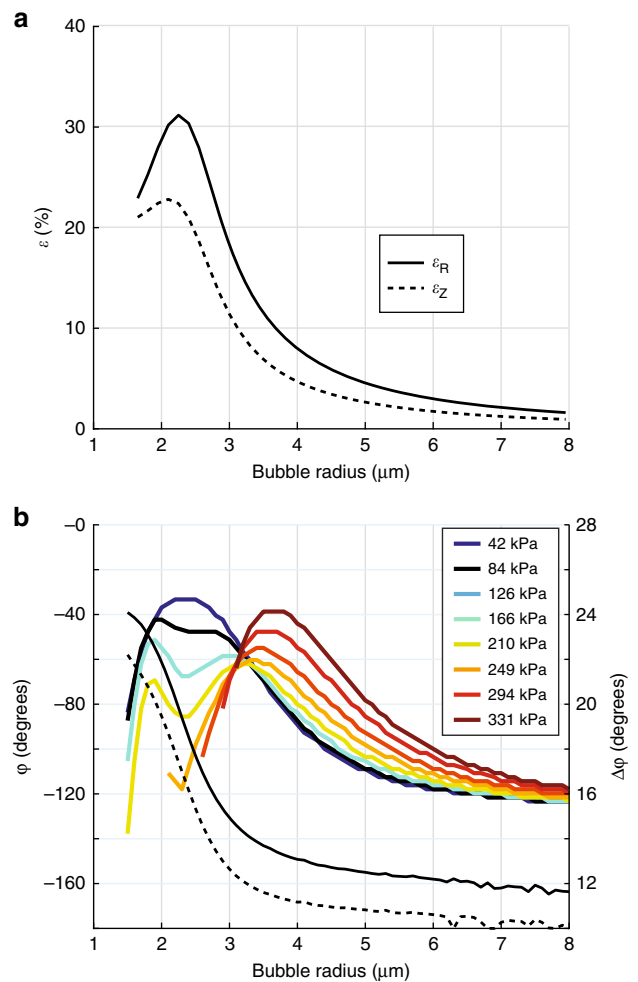
The amplitude of the volumetric oscillations and the oscillatory translations, as well as their phases, and their phase difference, follow directly from the simulation. Figure 5a displays the volumetric oscillation and oscillatory translation amplitudes as a function of the bubble radius at a driving pressure of 100 kPa and a frequency of 1 MHz. It is evident that it displays strong resonance behavior. Similarly, the corresponding phase of the simulated volumetric oscillations and oscillatory translations, Fig. 5b, displays the characteristics of a resonant system. In addition, Fig. 5b plots the calculated phase difference for different pressures. Note that the bubble size corresponding to the maximum phase difference is found to increase with increasing pressure.

Bubble streaming-induced transport. The transport distance $s(t)$ of a fluid element along the centerline (z-axis) is calculated by integrating the Lagrangian velocity of the particle, Eq. (7), from time zero to t:

$$s(t) = \int_0^t u(z(t))\,\mathrm{d}t. \quad (11)$$

The transport distance is measured directly from the high-speed fluorescence recordings.

Figure 6a plots the experimental transport distance vs. time. The integration in Eq. (11) is carried out over the duration of the ultrasound burst, in this case 100 µs. The calculated transport distance is valid for bubbles in a stationary oscillation regime and in a stationary streaming flow field, i.e. in the absence of transient effects, and with the bubble kept at a fixed location. Sometimes, and even more so at elevated pressures, the bubbles break-up, jet, pinch-off daughter bubbles or move rapidly along the substrate while disturbing the streaming field. For the targeted

Fig. 5 Non-spherical oscillation amplitude and phase. **a** The volumetric oscillation amplitudes ϵ_R (solid black line) and oscillatory translation amplitude ϵ_z (dashed black line) as a function of the bubble radius at a driving pressure of 84 kPa and a frequency of 1 MHz. **b** Phase φ (left y-axis) of the volumetric oscillations (solid black line) and oscillatory translations (dashed black line) for the same conditions as in (**a**). The colored lines denote the resulting phase difference $\Delta\varphi$ (right y-axis) between volumetric oscillations and oscillatory translations for different driving pressures

microbubbles that do fulfill the conditions of the model, the measured transport distance is plotted in Fig. 6c–e together with the predicted transport distance (see Supplementary Note 6 for details), where we find overall very good agreement. Note that the experimental results show some variability in the observed transport distance, owing to the large variations in the non-linear bubble response and subsequent second-order effects, which includes bubble streaming. Finally, coming back to the time evolution of the bubble streaming-induced transport, Fig. 6b shows the calculated transport distances at resonance, showing that most efficient transport is achieved within the first 200 µs and that the effect of longer pulse duration, and notably increased pressure, is only marginal, since a doubling of the pressure only leads to a 25% increase of the transport distance.

Discussion

The presence of a shell has two effects on bubble dynamics: an increased damping due to shell viscosity and an increased stiffness due to shell elasticity. Several models were proposed to account for bubble shells[42, 43]. The present model includes a shell viscosity (see Eq. (2)), which mainly increases the required
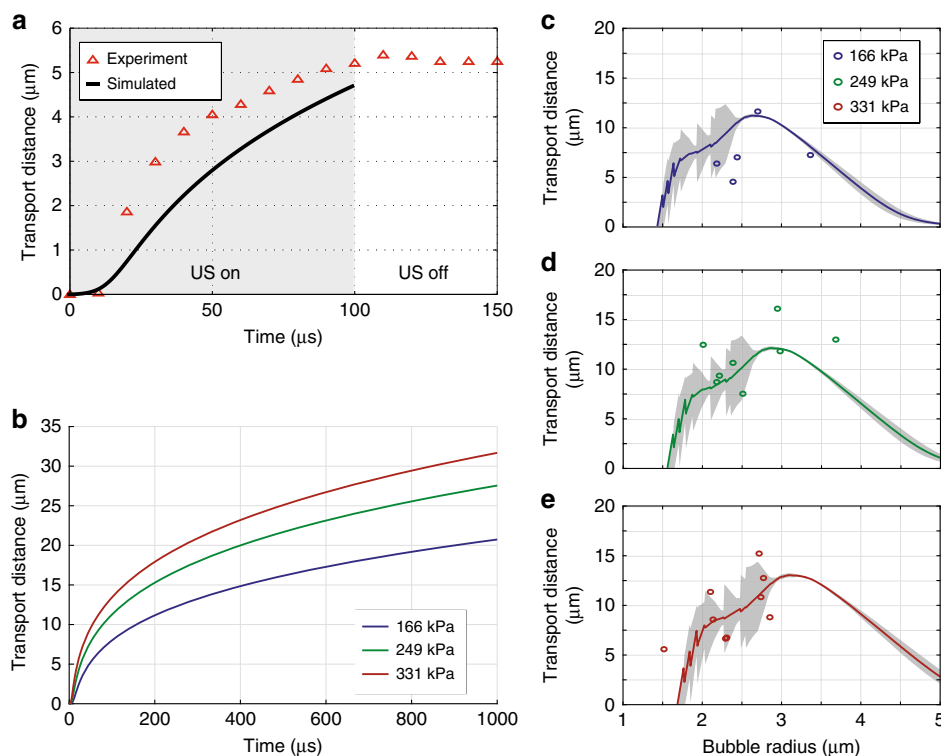
Fig. 6 Transport of the microbubble payload. **a** Experimental (red triangles) and computed (solid black line) transport distance vs. time plot of the fluorescent material shed by a 2.0 μm radius microbubble driven at a pressure of 84 kPa. **b** Calculated transport distance at resonance vs. time for acoustic pressures of 166, 249, and 331 kPa and 1 MHz excitation frequency. **c–e** Simulated (solid lines) and measured (circles) transport distance for microbubbles exposed to a 100-cycle, 1 MHz ultrasound burst of 166, 249, and 331 kPa. The gray areas denote the standard deviation of the scaled model for all pressures computed; see Supplementary Note 6

pressure to reach the same oscillation amplitude and has otherwise negligible impact on the response. Rigorously considering the shell elasticity for non-spherical oscillation is complex as the response of a lipid monolayer to bending and the phospholipids dynamics on the bubble surface at MHz rates and on the microscale is unknown. Here, the coating is almost entirely shed within the first few microseconds, and therefore shell elasticity is neglected to compute the streaming. Adding shell elasticity to our computation, according to the Marmottant model[31], induces a shift in the resonant radius but resulted in comparable surface reduction plots at resonance (Fig. 3a) and led to the same physical description of the shedding process. A contribution of shell elasticity was therefore not included.

The release of material from the bubble coating is often accompanied by the pinch-off of smaller submicron-sized bubbles. A direct implication is the immediate size reduction of the mother microbubble. This pinch-off process was also reported in earlier work[44, 45]. In the present experiments, these events were very difficult to control and highly irreproducible. It appears that the secondary bubbles carry some fluorescent shell material with them, while moving away from the bubble. Pinch-off occurred in about one third of the cases, with no obvious dependency on bubble size or oscillation amplitude.

For larger bubbles (≥4 μm) and higher pressures (≥350 kPa), jet formation was often observed. Such jets were reported before[46]: following asymmetrical collapse, the jet penetrates the bubble core and impinges onto the substrate. The role of jetting on cell poration is often discussed, but its resulting effects on the microbubble shell or on the delivery of a payload has received little attention. During collapse, the fluorescent coating appears to be following the jet, leading to its deposition onto the supporting substrate. Although jetting is not our present focus, this effect

could certainly be of further interest for drug delivery with microbubbles.

The present study was performed on a model drug inserted between the phospholipids that coat the microbubble. A previous study[27] has demonstrated that microbubbles loaded with liposomes or polymeric nanoparticles quantitatively display identical behavior when compared in terms of microbubble oscillation amplitude. Changing the type of payload is therefore not expected to change the conclusions presented here. The ability of the targeted microbubbles to deliver various payloads over a distance several times larger than their own size presents great potential for targeted drug delivery and theranostic applications.

The behavior of phospholipid molecules on the microbubble surface is highly complex and the subject of much attention from researchers in the field of interfacial chemistry. Quasi-static Langmuir trough measurements state that the shell should collapse when reducing the bubble size by only a few percent[26, 47]. It is however known not to hold for ultrasound-driven microbubbles, in particular due to the fast dynamical aspects[48]. On short timescales, the residence time of molecules at the interface will be related to the desorption potential barrier and to the viscosity associated with molecular motion[49]. Also, the compression of the phospholipids in a localized area of the surface can be expected to result in molecular transport along the shell, motion that is also subjected to molecular friction. Motion of individual molecules and the associated molecular processes remain to be explored. Interesting insights here may be provided, e.g. by molecular dynamic simulations.

Finally, this work highlights the importance of the substrate that supports the microbubble. Note that in the proposed model, the substrate is considered rigid in a fluid dynamical sense, which is justified by the very short length scales involved, as well as what

is observed in experiment. The results presented here improve our understanding of the delivery of a drug from targeted microbubbles and thereby our control over microbubble shedding. The present configuration of payload release along the symmetry axis of the adherent bubble can be highly efficient in small vessels and capillaries. However, this configuration may be suboptimal for sonoporation or sonothrombolysis, where the transport should preferentially be directed toward the target cells. In order to optimize drug delivery, next steps should extend the present work towards more compliant substrates, as found in vivo, and define more advanced strategies to control the transport direction.

Methods

Numerical methods. The set of second-order differential equations of Eq. (1) was solved numerically using the ODE113 solver in MATLAB (v. R2016b, The MathWorks, Natick, MA). The pressure inside the bubble, Eq. (2), was calculated from the summation of the individual segment volumes. The number of segments was varied between 20, sufficient for convergence of the model, and 100 for an optically pleasant rendering; see e.g. Supplementary Movies 4 and 5. The physical constants used for the simulation are as follows: density of water $\rho_\ell = 1000 \text{ kg m}^{-3}$, liquid viscosity $\mu_\ell = 1 \text{ mPa s}$, surface tension of water $\sigma_w = 72 \text{ mN m}^{-1}$, and polytropic exponent of the C_4F_{10} gas $\gamma = 1.05$. The damping contributions, including the more extended formalism for the thermal damping, were modeled along the work of Prosperetti[50]. The empirical damping term $\kappa = 2.3 \times 10^{-5} \text{ m}^2 \text{ s}^{-1}$ was fixed for all simulations. The acoustic driving pressure was increased from 42 to 331 kPa in nine steps with a frequency of 1 MHz.

Bubble preparation. Biotinylated microbubbles[6] were prepared by sonication. The coating was composed of DSPC (59.4 mol%; Sigma-Aldrich, Zwijndrecht, The Netherlands), polyoxyethylene-40 stearate (35.7 mol%; Sigma-Aldrich), DSPE-PEG (2000) (4.1 mol%; Avanti Polar Lipids, Alabaster, AL, USA) and DSPE-PEG(2000)-biotin (0.8 mol%; Avanti Polar Lipids). For fluorescence labeling, DiI (Molecular Probes, Eugene, OR, USA) was dissolved in ethanol and added to the solution before sonication.

Sample preparation. The topside of an OptiCell (Thermo Fisher Scientific, Waltham, MA, USA) was coated by adding 1 mL of 1 µg mL^{-1} solution of NeutrAvidin (Life Technologies Europe, Bleiswijk, The Netherlands) in phosphate-buffered saline (PBS) (Life Technologies Europe) 24 h prior to the experiment. The surface was then rinsed with PBS to remove all unbound proteins and incubated for 1 h with 1% bovine serum albumin (Sigma-Aldrich) to prevent unspecific binding. Afterwards, the surface was cut into rectangular pieces of 5 mm × 20 mm. Biotinylated microbubbles were injected into the tank and allowed to adhere to the surface by flotation for 5 min.

Experimental methods. The substrate was immersed in a water bath ($T \approx 22 \,^\circ\text{C}$), filled with demineralized water, under a 45° angle with respect to the vertical, and could be moved with a 3D micropositioning stage. A focused, single-element ultrasound transducer (C302, Panametrics, Waltham, MA, USA) with a center frequency of 1 MHz was fixed on one side of the water tank and used for insonation. A detailed schematic of the setup is given in Supplementary Note 7. For each recording, a single microbubble was exposed to a single ultrasound burst. The acoustic pressures were measured with a calibrated needle hydrophone (0.2 mm, Precision Acoustics, Dorchester, UK). Optical recordings were performed using a microscope equipped with a 20x water-immersion objective (LUMPFL, Olympus, Zoeterwoude, The Netherlands) that was fixed at a 45° angle relative to the vertical (with the optical axis parallel to the substrate). A continuous-wave diode laser (5 W, $\lambda = 532$ nm; Cohlibri, Lightline, Osnabrück, Germany) was focused onto the sample through the same objective, using a dichroic mirror. The laser light was gated using an acousto-optic modulator (AOTF.nC-VIS, AA Optoelectronic, Orsay, France) to generate a 500 µs laser pulse. Simultaneously, a KL 2500 LED light source (Schott, Mainz, Germany) was used to superimpose bright-field and fluorescence. High-speed recordings were acquired with a high-speed camera (SA-X, Photron, West Wycombe, UK), operating at 5000 to 50,000 fps. Ultra-high-speed imaging was performed with the Brandaris 128 camera[51] at frame rates ranging from 5 to 10 million fps. Using a beam splitter, 80% of the light was directed into the Brandaris camera, while the remaining 20% was directed towards the Photron camera. A test was performed for 12 targeted microbubbles recorded in a top-view configuration. Identical shedding was observed as compared to our previous study[27], demonstrating that the targeting did not significantly alter the process.

Analysis. The recordings were contrast-enhanced, and analyzed using a thresholding method in MATLAB to extract the bubble contours $R(\vartheta, t)$. The bubble volume was obtained by assuming axial symmetry. Due to the more complex aspect

of the released fluorescent material, the transport distance was extracted by manually selecting the center of the fluorescence patch in each frame of the recordings.

References

1. Minnaert, M. On musical air-bubbles and the sound of running water. *Philos. Mag.* **16**, 235–248 (1933).
2. Harvey, C. J., Pilcher, J. M., Eckersley, R. J., Blomley, M. J. K. & Cosgrove, D. O. Advances in ultrasound. *Clin. Radiol.* **57**, 157–177 (2002).
3. Overvelde, M. et al. Nonlinear shell behavior of phospholipid-coated microbubbles. *Ultrasound Med. Biol.* **36**, 2080–2092 (2010).
4. Chen, C. C. & Borden, M. A. The role of poly(ethylene glycol) brush architecture in complement activation on targeted microbubble surfaces. *Biomaterials* **32**, 6579–6587 (2011).
5. Lindner, J. R. et al. Noninvasive ultrasound imaging of inflammation using microbubbles targeted to activated leukocytes. *Circulation* **102**, 2745–2750 (2000).
6. Klibanov, A. L. et al. Detection of individual microbubbles of ultrasound contrast agents: imaging of free-floating and targeted bubbles. *Invest. Radiol.* **39**, 187–195 (2004).
7. Tinkov, S. et al. New doxorubicin-loaded phospholipid microbubbles for targeted tumor therapy: in-vivo characterization. *J. Control. Release* **148**, 368–372 (2010).
8. Lentacker, I., Geers, B., Demeester, J., De Smedt, S. C. & Sanders, N. N. Design and evaluation of doxorubicin-containing microbubbles for ultrasound-triggered doxorubicin delivery: cytotoxicity and mechanisms involved. *Mol. Ther.* **18**, 101–108 (2009).
9. Geers, B. et al. Self-assembled liposome-loaded microbubbles: the missing link for safe and efficient ultrasound triggered drug-delivery. *J. Control. Release* **152**, 249–256 (2011).
10. Kheirolomoom, A. et al. Acoustically-active microbubbles conjugated to liposomes: characterization of a proposed drug delivery vehicle. *J. Control. Release* **118**, 275–284 (2007).
11. Hope Simpson, D., Chin, C. T. & Burns, P. N. Pulse inversion Doppler: a new method for detecting nonlinear echoes from microbubble contrast agents. *IEEE Trans. Ultrason. Ferroelectr. Freq. Control* **46**, 372–382 (1999).
12. Sirsi, S., Feshitan, J., Kwan, J., Homma, S. & Borden, M. Effect of microbubble size on fundamental mode high frequency ultrasound imaging in mice. *Ultrasound Med. Biol.* **36**, 935–948 (2010).
13. Versluis, M. et al. Microbubble shape oscillations excited through ultrasonic parametric driving. *Phys. Rev. E* **82**, 026321 (2010).
14. Dollet, B. et al. Nonspherical oscillations of ultrasound contrast agent microbubbles. *Ultrasound Med. Biol.* **34**, 1465–1473 (2008).
15. Vos, H. J., Dollet, B., Versluis, M. & de Jong, N. Nonspherical shape oscillations of coated microbubbles in contact with a wall. *Ultrasound Med. Biol.* **37**, 935–948 (2011).
16. Fernández Rivas, D. et al. Localized removal of layers of metal, polymer, or biomaterial by ultrasound cavitation bubbles. *Biomicrofluidics* **6**, 34114 (2012).
17. Petit, B. et al. In vitro sonothrombolysis of human flood clots with BR38 microbubbles. *Ultrasound Med. Biol.* **38**, 1222–1233 (2012).
18. Li, T. et al. Passive cavitation detection during pulsed HIFU exposures of ex vivo tissues and in vivo mouse pancreatic tumors. *Ultrasound Med. Biol.* **40**, 1523–1534 (2014).
19. Graham, S. M. et al. Inertial cavitation to non-invasively trigger and monitor intratumoral release of drug from intravenously delivered liposomes. *J. Control. Release* **178**, 101–107 (2014).
20. Lipsman, N. et al. Initial experience of blood-brain barrier opening for chemotherapeutic-drug delivery to brain tumours by MR-guided focused ultrasound. *Neuro. Oncol.* **19**, vi9 (2017).
21. Wistuba, I. I., Gelovani, J. G., Jacoby, J. J., Davis, S. E. & Herbst, R. S. Methodological and practical challenges for personalized cancer therapies. *Nat. Rev. Clin. Oncol.* **8**, 135–141 (2011).
22. Pardridge, W. M. Vector-mediated drug delivery to the brain. *Adv. Drug Deliv. Rev.* **36**, 299–321 (1999).
23. Ganta, S., Devalapally, H., Shahiwala, A. & Amiji, M. A review of stimuli-responsive nanocarriers for drug and gene delivery. *J. Control. Release* **126**, 187–204 (2008).

24. Borden, M. A. et al. Influence of lipid shell physicochemical properties on ultrasound-induced microbubble destruction. *IEEE Trans. Ultrason. Ferroelectr. Freq. Control* **52**, 1992–2002 (2005).

25. O'Brien, J. P., Stride, E. & Ovenden, N. Surfactant shedding and gas diffusion during pulsed ultrasound through a microbubble contrast agent suspension. *J. Acoust. Soc. Am.* **134**, 1416–1427 (2013).

26. Kwan, J. J. & Borden, M. A. Lipid monolayer collapse and microbubble stability. *Adv. Colloid Interf. Sci.* **183**, 82–99 (2012).

27. Luan, Y. et al. Lipid shedding from single oscillating microbubbles. *Ultrasound Med. Biol.* **40**, 1834–1846 (2014).

28. Kooiman, K., Vos, H. J., Versluis, M. & de Jong, N. Acoustic behavior of microbubbles and implications for drug delivery. *Adv. Drug Deliv. Rev.* **72**, 28–48 (2014).

29. Keller, J. B. & Miksis, M. Bubble oscillations of large amplitude. *J. Acoust. Soc. Am.* **68**, 628–633 (1980).

30. Prosperetti, A. & Lezzi, A. Bubble dynamics in a compressible liquid. Part 1. First-order theory. *J. Fluid Mech.* **168**, 457–478 (1986).

31. Marmottant, P. et al. Model for large amplitude oscillations of coated bubbles accounting for buckling and rupture. *J. Acoust. Soc. Am.* **118**, 3499–3505 (2005).

32. Sarkar, K., Shi, W. T., Chatterjee, D. & Forsberg, F. Characterization of ultrasound contrast microbubbles using in vitro experiments and viscous and viscoelastic interface models for encapsulation. *J. Acoust. Soc. Am.* **118**, 539–550 (2005).

33. Lamb, H. *Hydrodynamics*, 6th edn (Cambridge University Press, Cambridge, 1932).

34. Doinikov, A. et al. Acoustic scattering from a contrast agent microbubble near an elastic wall of finite thickness. *Phys. Med. Biol.* **56**, 6951–6967 (2011).

35. Hay, T. A., Ilinskii, Y. A., Zabolotskaya, E. A. & Hamilton, M. F. Model for bubble pulsation in liquid between parallel viscoelastic layers. *J. Acoust. Soc. Am.* **132**, 124–137 (2012).

36. Overvelde, M. et al. Dynamics of coated microbubbles adherent to a wall. *Ultrasound Med. Biol.* **37**, 1500–1508 (2011).

37. Helfield, B. L., Leung, B. Y. C. & Goertz, D. E. The effect of boundary proximity on the response of individual ultrasound contrast agent microbubbles. *Phys. Med. Biol.* **59**, 1721–1745 (2014).

38. Pierce, A. *Acoustics—An Introduction to its Physical Principles and Applications* (McGraw-Hill Book Co, New York, 1981).

39. Helfield, B. L. & Goertz, D. E. Nonlinear resonance behavior and linear shell estimates for Definity and MicroMarker assessed with acoustic microbubble spectroscopy. *J. Acoust. Soc. Am.* **133**, 1158–1168 (2013).

40. Marmottant, P. & Hilgenfeldt, S. Controlled vesicle deformation and lysis by single oscillating bubbles. *Nature* **423**, 153–156 (2003).

41. Longuet-Higgins, M. S. Viscous streaming from an oscillating spherical bubble. *Proc. R. Soc. Lond., Ser.* **A454**, 725–742 (1998).

42. Doinikov, A. A. & Bouakaz, A. Review of shell models for contrast agent microbubbles. *IEEE Trans. Ultrason. Ferroelectr. Freq. Control* **58**, 981–993 (2011).

43. Faez, T. et al. 20 years of ultrasound contrast agent modeling. *IEEE Trans. Ultrason. Ferroelectr. Freq. Control* **60**, 7–20 (2013).

44. Thomas, D. H. et al. The "quasi-stable" lipid shelled microbubble in response to consecutive ultrasound pulses. *Appl. Phys. Lett.* **101**, 071601 (2012).

45. Cox, D. J. & Thomas, J. L. Rapid shrinkage of lipid-coated bubbles in pulsed ultrasound. *Ultrasound Med. Biol.* **39**, 466–474 (2013).

46. Brennen, C. E. *Cavitation and Bubble Dynamics* (Cambridge Univ. Press, New York, 2014).

47. Lozano, M. M. & Longo, M. L. Complex formation and other phase transformations mapped in saturated phosphatidylcholine/DSPE-PEG2000 monolayers. *Soft Matter* **5**, 1822–1834 (2009).

48. Segers, T., de Rond, L., de Jong, N., Borden, M. & Versluis, M. Stability of monodisperse phospholipid-coated microbubbles formed by flow-focusing at high production rates. *Langmuir* **32**, 3937–3944 (2016).

49. Hosny, N. A. et al. Mapping microbubble viscosity using fluorescence lifetime imaging of molecular rotors. *Proc. Natl. Acad. Sci. USA* **110**, 9225–9235 (2013).

50. Prosperetti, A. Application of the subharmonic threshold to the measurement of the damping of oscillating gas bubbles. *J. Acoust. Soc. Am.* **61**, 11–16 (1977).

51. Gelderblom, E. C. et al. Brandaris 128 ultra-high-speed imaging facility: 10 years of operation, updates, and enhanced features. *Rev. Sci. Instr.* **83**, 103706 (2012).

Acknowledgements

Author contributions

G.L., M.V., and N.dJ. designed the study. G.L., Y.L., E.G., H.D., I.L., F.M., and M.V. performed the research. G.L., Y.L., E.G., H.D., I.L., M.V., B.D., and F.M. wrote the manuscript.

Additional information

Supplementary information accompanies this paper at https://doi.org/10.1038/s42005-018-0020-9.

Competing interests: The authors declare no competing interests.

Reprints and permission information is available online at http://npg.nature.com/reprintsandpermissions/

Publisher's note: Springer Nature remains neutral with regard to jurisdictional claims in published maps and institutional affiliations.